Virus Research 341 (2024) 199319

Contents lists available at ScienceDirect

Virus Research

journal homepage: www.elsevier.com/locate/virusres

Divergent pathogenetic outcomes in BALB/c mice following Omicron subvariant infection

John M. Powers [a,*], Sarah R. Leist [a], Michael L. Mallory [a], Boyd L. Yount [a], Kendra L. Gully [a], Mark R. Zweigart [a], Alexis B. Bailey [a], Timothy P. Sheahan [a,b], Jack R. Harkema [c], Ralph S. Baric [a,b]

[a] Department of Epidemiology, Gillings School of Global Public Health, University of North Carolina, Chapel Hill, NC 27599, USA
[b] Department of Microbiology and Immunology, University of North Carolina at Chapel Hill, Chapel Hill, NC, USA
[c] Department of Pathobiology & Diagnostic Investigation, Michigan State University, East Lansing, MI, USA

ARTICLE INFO

Keywords:
SARS-CoV-2
XBB.1
XBB.1.5
BQ.1.1
Pathogenesis
Mouse models

ABSTRACT

Following the emergence of B.1.1.529 Omicron, the SARS-CoV-2 virus evolved into a significant number of sublineage variants that possessed numerous mutations throughout the genome, but particularly within the spike glycoprotein (S) gene. For example, the BQ.1.1 and the XBB.1 and XBB.1.5 subvariants contained 34 and 41 mutations in S, respectively. However, these variants elicited largely replication only or mild disease phenotypes in mice. To better model pathogenic outcomes and measure countermeasure performance, we developed mouse adapted versions (BQ.1.1 MA; XBB.1 MA; XBB.1.5 MA) that reflect more pathogenic acute phase pulmonary disease symptoms of SARS-CoV-2, as well as derivative strains expressing nano-luciferase (nLuc) in place of ORF7 (BQ.1.1 nLuc; XBB.1 nLuc; XBB.1.5 nLuc). Amongst the mouse adapted (MA) viruses, a wide range of disease outcomes were observed including mortality, weight loss, lung dysfunction, and tissue viral loads in the lung and nasal turbinates. Intriguingly, XBB.1 MA and XBB.1.5 MA strains, which contained identical mutations throughout except at position F486S/P in S, exhibited divergent disease outcomes in mice (Ao et al., 2023). XBB.1.5 MA infection was associated with significant weight loss and ~45 % mortality across two independent studies, while XBB.1 MA infected animals suffered from mild weight loss and only 10 % mortality across the same two independent studies. Additionally, the development and use of nanoluciferase expressing strains provided moderate throughput for live virus neutralization assays. The availability of small animal models for the assessment of Omicron VOC disease potential will enable refined capacity to evaluate the efficacy of on market and pre-clinical therapeutics and interventions.

1. Introduction

The severe acute respiratory syndrome coronavirus 2 (SARS-CoV-2) virion contains a ~30 kb positive-sense single-stranded RNA genome that encodes 16 non-structural proteins (nsp1–nsp16), four structural proteins (spike, membrane, envelope, and nucleocapsid), and at least six accessory proteins (Kim et al., 2020; Jungreis et al., 2021). SARS-CoV-2 infection results in COVID-19 disease, which has caused hundreds of millions of infections and millions of deaths globally (https://covid19.who.int/). Although significant international efforts have produced several effective vaccines, monoclonal antibodies (mAbs), and small molecule inhibitors that reduce the spread and severity of infection, new variants of interest (VOI) and variants of concern (VOC) emerge periodically, circulate globally, and erode countermeasure performance. After emerging in Botswana and South Africa in November 2021, the Omicron BA.1 VOC was shown to be highly transmissible and infectious and capable of escaping existing natural infection and vaccine-induced immunity. Ever since, a considerable number of Omicron sublineage VOC have continued to emerge at regular intervals like XBB.1, XBB.1.5, and BQ.1.1, which are defined by differences in general disease severity, infectivity, and immune evasion (Simon-Loriere and Schwartz, 2022; Silva Junior et al., 2023; Gili and Burioni, 2023). These Omicron lineage variants continue to accrue mutations throughout the spike glycoprotein (S) gene, with large numbers appearing in the receptor binding domain (RBD) and the receptor binding motif (RBM).

Prior to the emergence of Omicron BA.5, amino acid position F486

* Corresponding author.
E-mail address: jpowers@unc.edu (J.M. Powers).

https://doi.org/10.1016/j.virusres.2024.199319
Received 30 September 2023; Received in revised form 2 January 2024; Accepted 12 January 2024
Available online 19 January 2024

was highly conserved (Zhang et al., 2023). As BQ.1.1, XBB.1, and XBB.1.5 all express different amino acid mutations in the S protein at position F486 (V, S, & P respectively), we probed the role of this residue on virus infectivity and pathogenicity using aged BALB/c mice. Spike glycoprotein RBD/RBM mutations are capable of subtly altering human angiotensin-converting enzyme 2 (hACE2) receptor interactions, entry efficiency, and transmissibility (Lan et al., 2020). Previous studies have identified an important role for position S F486 in binding interactions with hACE2 and mouse angiotensin-converting enzyme 2 (*mACE2*) (Pach et al., 2021; Wan et al., 2020; Adams et al., 2021; Ni et al., 2023; Huang et al., 2020). Further, these mutations potentially altered pathogenic outcomes in small animal models of human disease. As XBB.1 MA and XBB.1.5 MA contain an identical genetic backbone except at position S F486, these recombinant viruses provided a model to define the potential impact of mutations at this site on *in vitro* and *in vivo* phenotypes. Additionally, mutations within the viral RBD also enable escape from pre-existing neutralizing antibodies due to changes at key antigenic epitopes, supporting the hypothesis that new serotypes are emerging that are antigenically distinct from the original Wuhan ancestral strain (Tsai et al., 2021; Greaney et al., 2021; Starr et al., 2021). Along with RBD and RBM mutations that potentially alter ACE2 receptor usage, other mutations alter proteolytic processing by transmembrane protease serine 2 (TMPRSS2), furin protease, and potentially other proteases, changing viral-cell membrane fusion, entry and infection phenotypes (Zhou et al., 2020; Letko et al., 2020; Hoffmann et al., 2020).

Using aged female BALB/c mice that are highly permissive for mouse adapted SARS-CoV-2 and mouse adapted VOC infections, we compared and contrasted clinical disease phenotypes like weight loss, survival, lung dysfunction, and tissue viral loads after Omicron sublineage variant infection (Dinnon et al., 2020; Leist et al., 2020; Feng et al., 2023; Martinez et al., 2021). In the backdrop of demonstrating the development of small animal models of disease which can utilize commonly available laboratory wildtype and transgenic mice, we demonstrate a role for S gene F486 mutations in viral pathogenesis and provide models for a rigorous evaluation of clinical and pre-clinical therapeutics and countermeasures, as well as expanding our knowledge on the impact of accrued mutations within the S glycoprotein gene. Further, we explored the differences elicited by these variants when compared to our ancestral MA10 virus finding that a log higher dose of virus inoculum was required to elicit similar disease phenotypes for BQ.1.1 and XBB.1.5 implicating that infection with Omicron VOCs requires a higher initial viral dose to drive significant pathogenesis. Supporting this hypothesis, even at a log higher dose, the disease state elicited by XBB.1 was still only mildly pathogenic and less severe than the other viruses tested. In parallel, we also designed full-length reporter viruses that expressed nanoluciferase (nLuc) in place of ORF7a, providing a live virus nLuc reporter neutralizing assay that can be used to screen monoclonal antibodies, serum, and anti-viral drugs. Using banked serum from vaccinated BALB/c mice we identified strong neutralization against the parental D614G nLuc virus, while greater than a log reduction in neutralizing capability against the BQ.1.1, XBB.1, and XBB.1.5 nLuc viruses was noted.

2. Materials and methods

2.1. Virus and cells

Viruses were designed using our previously published infectious clones for wildtype SARS-CoV-2 or a mouse adapted SARS-CoV-2 MA10 (MA10) or SARS-CoV-2 D614G nLuc (D614G nLuc) (GenBank accession numbers: MT952602.1 and MT461669) (Leist et al., 2020). Omicron S glycoprotein expressing variants designed through reverse genetics have been deposited at GenBank under accension numbers OR887433 & OR887434 (BQ.1.1), OR887435 & OR887436 (XBB.1), and OR887437 & OR887438 (XBB.1.5). All viruses contained a marker mutation in Nsp12 to distinguish from naturally circulating SARS-CoV-2 viruses through the addition of a T15102A mutation to remove a naturally occurring SacI restriction site. The virus backbones for MA10 and D614G nLuc were engineered to encode various Omicron spikes and recombinant viruses were recovered after transfection into cells using previously described techniques (Dinnon et al., 2020; Leist et al., 2020).

Mutations for BQ.1.1 S glycoprotein included: T19I, L24S, Δ25–27, Δ69 & 70, G142D, V213G, G339D, R346T, S371F, S373P, S375F, T376A, D405N, R408S, K417N, N440K, K444T, L452R, N460K, S477N, T478K, E484A, F486V, Q498R, N501Y, Y505H, D614G, H655Y, N679K, P681H, N764K, D796Y, Q954H, N969K. Mutations in the XBB.1 S glycoprotein included: T19I, L24S, Δ25–27, V83A, T95I, G142D, Δ144, H146Q, Q183E, V213E, G252V, G339H, R346T, L368I, S371F, S373P, S375F, S376A, D405N, R408S, K417N, N440K, V445P, G446S, N460K, S477N, T478K, E484A, F486S, F490S, Q498R, N501Y, Y505H, D614G, H655Y, N679K, P681H, N764K, D796Y, Q954H, N969K. To build XBB.1.5, the unique S486P change was introduced into XBB.1. Full length live infectious viruses were then recovered on either the MA10 backbone for mouse studies, or on a WA-1 isolate backbone where ORF7a was replaced with nanoluciferase for live-virus neutralization assays (Dinnon et al., 2020; Hou et al., 2020a; Leist et al., 2020).

Viruses were derived following systematic cDNA assembly of the infectious clone fragments, followed by *in vitro* transcription with mMessage Machine T7 polymerase (ThermoFisher). Additionally, a separate reaction using a T7 promoter upstream of the nucleocapsid gene was used to produce nucleocapsid mRNA. Prior to electroporation, Vero E6 cells over-expressing human TMPRSS2/ACE2 in Opti-MEM (Gibco), a gift from Adrian Creanga and Barney Graham at the Vaccine Research Center (NIAID, Bethesda, MD), were mixed with the full-length mRNA as well as the nucleocapsid mRNA. Cells and RNA were electroporated under the following conditions: 450 Vs, 50 microfarads, 4 pulses and allowed to recover for 10 min before plating into a T75 flask with 10 mL of Dulbecco's modified Eagle's medium (DMEM; Gibco) with Fetal Bovine Serum (FBS, Hyclone), and 1X antibiotic/antimycotic (Gibco). Cells were grown under 5 % CO_2 at 37 °C and checked for CPE at 24 h post infection (hpi). Viruses were harvested when ~75 % of the cells on the flask demonstrated cytopathic effects (CPE) and passage 0 stocks (p0) were centrifuged at 500 xg and stored at −80 °C in 1 ml aliquots. To make working stocks, 1 mL of p0 virus was inoculated into a ~90 % confluent T175 flask seeded with Vero E6 over-expressing human TMPRSS2/ACE2 in 24 mL of culture media. Virus supernatants were harvested when ~75 % of the cells demonstrated CPE, after which the infectious media was spun down, aliquoted, and frozen at −80 °C.

The viral titer of the stock was determined via plaque assay. Briefly, virus stock was serially diluted ten-fold and inoculated onto confluent monolayers of Vero E6 cells in 6 well plates. Plates were incubated for 1 hour with rocking every 15 min. Subsequently, DMEM with FBS and 1X antibiotic/antimycotic and 0.8 % agarose was applied as an overlay. Plaques were visualized at 3 days post infection via staining with neutral red dye. Virus genomic integrity and sequence were confirmed by deep-sequencing cDNA from viral RNA on an Illumina® MiSeq sequencer.

Growth curve analysis was conducted on Vero E6 cells in a six well dish where three wells were inoculated at a multiplicity of infection of 0.001 plaque forming units (PFU) per cell and culture media was harvested at 96 h post infection. The viral supernatant was clarified by centrifugation at 500 xg and then frozen at −80 °C. Viral titers were determined using the above described plaque assay method.

2.2. Mice and in vivo infections

Female 10 – 12-month-old BALB/c mice were obtained from Envigo (strain 047). Mice were infected intranasally under ketamine/xylazine anesthesia with doses between 1×10^4 to 1×10^5 PFU in 50 μL as indicated. Body weight and pulmonary function by whole body plethysmography (Buxco respiratory solutions, DSI Inc.) were monitored daily. Weight loss was tracked across all cohort members for the

duration of the study, while survival and lung function were studied on a subset of five mice that were harvested at 7-days post infection (dpi). At indicated timepoints, a subset of approximately five mice were euthanized by isoflurane overdose. Serum samples were harvested for antibody titer, while the mouse left lung lobe was used for histopathological analysis, and the lower right lobe was used for determining virus titer. Titer samples were stored at −80 °C, and histopathology samples stored at 4 °C in 10 % phosphate buffered formalin (Fisher). Serum was collected into Microtainer® SST™ Blood Collection Tubes and allowed to clot. Clotted blood was then spun for 10 min at 10,000 xg. Clarified sera was then collected and stored at −80 °C.

Macroscopic lung discoloration scores were based on the number and severity of visible lung surface discoloration at the time of harvest (e.g., dark red vs. anatomical pink coloring). Briefly, upon sacrifice, once the chest cavity was opened, each lung lobe was scored by qualitative metrics to quantify the prevalence of lung discoloration by analysis of the left and 3 major right lung lobes. A score of 0.5 equates to half of a lobe displaying dark red discoloration, 1 to a whole lobe, and so forth, with a score of 4 representing involvement of all lung lobes in discoloration when compared to anatomical pink coloration of the lungs.

2.3. Vaccinated mouse serum for neutralization assays

Banked serum from 10–12-month-old female BALB/c mice vaccinated with a prime & boost regimen (boost 4 weeks post-prime, final bleed 4 weeks post-boost) was utilized for assessment of neutralizing antibody evasion. Mice were vaccinated intramuscularly into each thigh with 25 μL (50 μL total) of a PBS solution containing 1 μg S2P protein with 250 μg Aluminum Hydroxide adjuvant. The S2P spike stabilized protein vaccine included the Wuhan SARS-CoV-2 S gene sequence. After vaccination and boost, blood was collected either from non-terminal cheek bleeds or terminal thoracic aorta dissection into BD Microtainer® SST™ Blood Collection Tubes and allowed to clot. Clotted blood was then spun for 10 min at 10,000 xg. Clarified sera was then collected and stored at −80 °C. Prior to testing, sera was thawed and heat-inactivated at 56 °C for 30 min and debris were pelleted by spinning at 10,000 xg for 10 min in a microcentrifuge.

2.4. Nanoluciferase based neutralization assays

Heat-inactivated serum was diluted 1:20 by adding 11.25 μL of sera to 213.75 μL Minimum Essential Media (MEM) supplemented with 5 % FBS and 1X penicillin & streptomycin. Sera was then further diluted via 1:3 serial dilutions seven times by adding 75 μL of the previous dilution into 150 μL of media. Then, 150 μL of media containing 16,000 PFU/mL of nLuc virus was mixed with the diluted antibodies and allowed to incubate for 1 hr at 37 °C, after which 100 μL of the virus + antibody mix was added to individual wells in a 96 well plate seeded 24 h prior with 2×10^4 Vero C1008 cells for a final 800 PFU virus per well. Plates for D614G nLuc were incubated for 24–30 hrs, while plates for Omicron nLuc variants were incubated for 44–48 hrs at 37 °C with 5 % CO2. After incubation, luciferase activity was measured with the Nano-Glo Luciferase Assay System (Promega) according to the manufacturer specifications. Inhibitory concentrations were defined as the dilution at which a 50 % reduction in RLU was observed relative to the virus (no antibody or serum) control.

2.5. Histopathology and antigen staining

Mouse lungs were fixed for 7 days in 10 % phosphate buffered formalin, paraffin embedded, and sectioned at 5 μm. Sectioned tissue was stained with hematoxylin and eosin, and immunohistochemistry for the SARS-CoV-2 nucleocapsid was conducted using anti-SARS nucleocapsid antibody (NB100–56,576, Novus Biologicals) on deparaffinized sections on the Ventana Discovery Ultra platform (Roche). Histologic whole glass slides with stained lung tissue sections were digitally scanned using a VS200 Research Slide Scanner (Olympus, Center Valley, PA). Microscopic examination of digitized whole lung sections for virus-induced histopathology was conducted by a board-certified veterinary pathologist without knowledge of individual animal viral exposures (*blinded* assessment).

2.6. Statistical analysis

Statistical analysis was performed using GraphPad Prism 10. Statistical significance was determined by two-way ANOVA with Tukey's multiple comparison test for weight loss PenH, Rpef, and EF50 values; Kruskal-Wallis non-parametric test with Dunn's correction for lung discoloration; and one-way ANOVA with Tukey's multiple comparison test for tissue titers. * = $p < 0.05$, ** = $p < 0.01$, *** = $p < 0.001$, **** = $p < 0.0001$. Group numbers are listed in the text, with all cohorts starting at 5 members at the time of infection. Error bars represent standard error of the mean. Figure panels 1A and 5A – D utilize horizontal bars in the color of the virus with asterisk color.

2.7. Ethics and containment procedures

All recombinant viruses were approved by the University of North Carolina at Chapel Hill Institutional Review Board under Schedule G 78,684, 115,102, and 115,101. All animal work was approved by Institutional Animal Care and Use Committee at University of North Carolina at Chapel Hill under protocol 20–114 and 23–085 according to guidelines outlined by the Association for the Assessment and Accreditation of Laboratory Animal Care and the U.S. Department of Agriculture. All recombinant viruses were reviewed by the UNC IRB and virus studies were performed in animal biosafety level 3 facilities wearing a PAPR, Tyvek suits, Tyvek aprons and booties, and double gloves at University of North Carolina at Chapel Hill.

3. Results

3.1. Development of Omicron sublineage variant infectious clones

Using reverse genetics, we recovered SARS-CoV-2 viruses displaying S glycoproteins representative of BQ.1.1, XBB.1, and XBB.1.5 **(Supplemental Fig. 1 A – C)** (Zabidi et al., 2023). The recombinants were isolated either using a mouse adapted backbone (BQ.1.1 MA, XBB.1 MA, and XBB.1.5 MA)**(Supplemental Fig. 1D)**, or a wildtype backbone where ORF7a was replaced by a nano-luciferase cassette (BQ.1.1 nLuc, XBB.1 nLuc, and XBB.1.5 nLuc) as previously described by our group (Leist et al., 2020; Hou et al., 2020). Growth curve analysis identified that at 96-hours post infection (hpi) maximal titers were significantly reduced by at least 1 to 1.5 logs when compared to the parental D614G nLuc and MA10 viruses **(Supplemental Fig. 2A)**.

3.2. In vitro assessment of neutralizing capacity of vaccinated mouse sera by nanoluciferase assay

Twenty BALB/c mice were inoculated and then boosted with 1 μg of a Wuhan strain stabilized spike glycoprotein (S2P) vaccine adjuvanted with 250 μg of aluminum hydroxide (boost 4 weeks post-prime, challenge 4 weeks post-boost). Using heat-inactivated serum, we established a nLuc assay to determine the neutralization titers against SARS-CoV-2 D614G nLuc, BQ.1.1 nLuc, XBB.1 nLuc, and XBB.1.5 nLuc. To determine the linear range of the assay, nLuc expression was first measured after infecting cells with progressively more infectious virus and evaluating the intensity of the nanoluciferase expression at ~24-, 36-, and 48-hpi, including virus only controls **(Supplemental Fig. 2B)**. These studies revealed that 800 PFU remained comfortably within the linear stage of the curve and provided relatively uniform counts with over a ~2 log dynamic range at ~24-hpi for D614G **(Supplemental Fig. 2B, top left, blue dots)**, and ~48-hpi for the Omicron sublineage viruses, as

compared to background **(Supplemental Fig. 2B, top right and bottom row, orange diamonds)**. Background luciferase signal in the virus stocks were determined using wells lacking cells across the same timepoints **(Supplemental Fig. 2B, red octagon, grey square, and pink circle).**

After establishing an optimal assay, Wuhan S2P mouse vaccine sera was interrogated for live virus neutralization potential. Not surprisingly, the homotypic D614G nLuc strain was most sensitive to neutralization, with a mean ID_{50} value of 1694, although significant variation was noted in the cohort (SEM = 617.8). In contrast, significant reductions in neutralization potential were consistently observed against the three Omicron variants, resulting in ID_{50} values of 134.4 (SEM = 56.3), 53.2 (SEM = 23.9), and 26.5 (SEM = 4.9) for BQ.1.1, XBB.1, and XBB.1.5 respectively ($p = 0.023$, $p = 0.0002$, $p < 0.0001$ respectively compared to D614G). Samples that failed to neutralize were set at half the limit of detection (dashed line) **(Supplemental Fig. 2C)**. These data are consistent with earlier work demonstrating the significant antigenic distance between ancestral Wuhan and the more contemporary Omicron strains (Mykytyn et al., 2023; van der Straten et al., 2022).

3.3. *In vivo pathogenesis in BALB/c mice*

Compared to the Wuhan and early VOC strains like alpha and delta, Omicron related strains are typically highly or partially attenuated in mice and hamsters, depending on the VOC (Halfmann et al., 2022; Liu et al., 2022; Shuai et al., 2023). The MA10 strain causes 90 to 100 % mortality at a 10^4 or 10^5 PFU dose in aged BALB/c mice by day 4 (Leist et al., 2020). In order to assess the pathogenic potential of BQ.1.1 MA, XBB.1 MA, and XBB.1.5 MA, cohorts of fifteen female 11-12 months old aged mice were infected intranasally (50 μl) with 10^5 PFU of virus, as well as a control group inoculated with an equivalent volume of PBS. Prior to infection, cohorts of five mice from each infection group were selected for sacrifice at 2-, 4-, or 7-dpi. Each day, surviving cohort members were monitored for weight loss and mortality.

3.3.1. *Weight loss*

After infection, BQ.1.1 MA infected cohorts experienced a significant and persistently worsening disease phenotype over time and all mice in the cohort experienced rapid and sustained weight loss starting at 2-dpi with no trend towards recovery **(**Fig. 1**A, red line with circles)**. Mortality was either sudden or animals were euthanized as they approached 30 % weight loss due to humane euthanasia criteria. Mice also displayed hunching and lethargy as weight loss progressed. Similar trajectories and disease symptoms were observed for XBB.1.5 MA infected mice, achieving a peak mean weight loss of 25 %, with a slight trend towards weight gain noted at 7-dpi **(**Fig. 1**A, green line with circles)**. In contrast, significantly milder clinical disease phenotypes were observed in XBB.1 MA infected animals, which only experienced ~10 % body weight loss by days 2 – 4. Thereafter, mice began recovering and approached pre-infection body weights by 7-dpi **(**Fig. 1**A, purple line with circles)**. Minimal hunching and lethargy were noted in the XBB.1 cohort of mice.

In contrast, PBS mock infected mice showed consistent body weights across the period of observation, only losing 1.6 % of their starting weight **(**Fig. 1**A, black line with circles)**. When effects of each virus were compared at 4-dpi, both BQ.1.1 and XBB.1.5 group mean weights were significantly reduced when compared to XBB.1 (red bar with purple asterisks, green bar with purple asterisks, $p < 0.0001$). Through day 7, XBB.1.5 group mean body weights continued to remain significantly reduced when compared to XBB.1 (green bar with purple asterisks, $p < 0.0001$).

3.3.2. *Mortality*

The panel of Omicron S VOC demonstrated different mortality rates through 7-dpi. Under identical conditions, BQ.1.1 MA and XBB.1.5 MA caused 100 and 60 % mortality respectively while XBB.1 MA was significantly different as all animals survived through 7-dpi (Fig. 1**B**). For mice in the BQ.1.1 MA cohort, mortality was first observed at 3-dpi with a loss of all mice by 6-dpi due to infection elicited disease (4 of 5) or because they approached 30 % weight loss and/or humane euthanasia experiment endpoints (1 of 5) **(**Fig. 1**B, red line)**. As with weight loss phenotypes, mortality for XBB.1.5 MA was slightly decreased as compared to BQ.1.1 MA as only three of five from the observation cohort died of infection elicited disease **(**Fig. 1**B, green line)**. In contrast, all five observation cohort XBB.1 MA infected mice survived infection **(**Fig. 1**B, purple line)**. No mortality was observed within the PBS control cohorts either **(**Fig. 1**B, dot & dash black line)**.

3.3.3. *Gross lung discoloration*

Gross lung discoloration, a macroscopic observation of lung tissue coloration changes associated with inflammation, edema, and diffuse alveolar damage, was assessed at 2-, 4-, and 7-dpi at the time of tissue harvest. Discoloration was scored on a scale from 0 to 4 based on the incidence of discoloration of the four major lung lobes from innate anatomical pink to dark crimson colors. Among the mice infected with BQ.1.1 MA, progressively worsening discoloration was observed, increasing from an average of 0.9 (SEM = 0.78), $N = 5$) at 2-dpi to 3.33 (SEM = 0.67, $N = 3$) at 4-dpi **(**Fig. 1**C, red circles)**. In the absence of survivors at 7-dpi, no observations were recorded. Evaluation of XBB.1.5 MA infected mice identified widely varying levels of discoloration severity. While little if any discoloration was observed at 2-dpi ($N = 5$), the 4- and 7-dpi groups demonstrated a mean score of 2.25 (SEM = 1.75, $N = 2$) and 1.5 (SEM = 1, $N = 2$), respectively **(**Fig. 1**C, green circles)**. Examination of lung tissue of XBB.1 MA infected mice at the time of harvest again identified with little if any observable discoloration at 2-dpi, and minimal discoloration scores that approached 1 at 4- and 7-dpi, respectively (day 4 = 0.8, SEM = 0.56, $N = 5$; and day 7 = 1.1, SEM = 0.43, $N = 5$) **(**Fig. 1**C, purple circles)**. No discoloration was observed in members of the PBS control group at any point, indicating that discoloration was associated with virus infection and host inflammatory and reparative functions not due to volume of fluid delivered.

3.3.4. *Tissue viral loads*

Tissue viral loads were determined in the lungs of surviving mice at either 2-, 4-, or 7-dpi **(**Fig. 1**D)**, or nasal turbinates **(**Fig. 1**E)**. In comparison to the tissue viral loads after 10^4 MA10 infection in similarly aged mice, lung viral titers for the three omicron S VOC were reduced by at least 1 log across all timepoints (Leist et al., 2020). In contrast, the Omicron variants each displayed strikingly elevated nasal titers and retention in the nasal epithelium at 2- and 4-dpi when compared to MA10. For BQ.1.1 MA infected mice, maximal viral replication was achieved in both tissues at 2-dpi, achieving titers of 1.55×10^6 PFU/mL (SEM = 8.6×10^5, $N = 5$) in lung tissue and 1.02×10^6 PFU/mL (SEM = 6.06×10^5, $N = 5$) in nasal tissues. Virus titers in the lung decreased by nearly 2 logs by 4-dpi, approaching 2.17×10^4 PFU/mL (SEM = 1.86×10^3, $N = 3$) in the lung. At 4-dpi, nasal titers remained high, with a reduction of about 1 log to 1.88×10^5 PFU (SEM = 6.07×10^4, $N = 3$).

Like BQ.1.1 MA, elevated virus replication was also observed in XBB.1.5 MA infected mice with maximal lung (1.78×10^6 PFU/mL, SEM = 4.06×10^5, $N = 5$) and nasal titers (1.60×10^6 PFU/mL, SEM = 1.07×10^6, $N = 5$) achieved at 2-dpi (Fig. 1**D** & **E**). Reduction in viral load was observed in both the lung and nasal tissues at 4-dpi. Although mean lung titers were reduced by ~1 log, nasal titers still remained high and approached 10^6 PFU/mL. By 7-dpi, robust clearance was observed in the tissue samples from both the lung and nasal turbinates. Throughout the course of the experiment, viral loads for XBB.1 MA were significantly reduced by almost a log when compared with BQ.1.1 MA and XBB.1.5 MA, respectively. In fact, XBB.1 titers in both the lungs and nasal turbinates was significantly reduced when compared to XBB.1.5 at 2-dpi ($p < 0.01$ and $p < 0.05$ respectively), mirroring the reduced disease phenotypes observed for weight loss and mortality. Maximal XBB.1 lung titers reached 2.8×10^5 PFU/mL (SEM = 7.56×10^4, $N = 5$) at 2-dpi (p

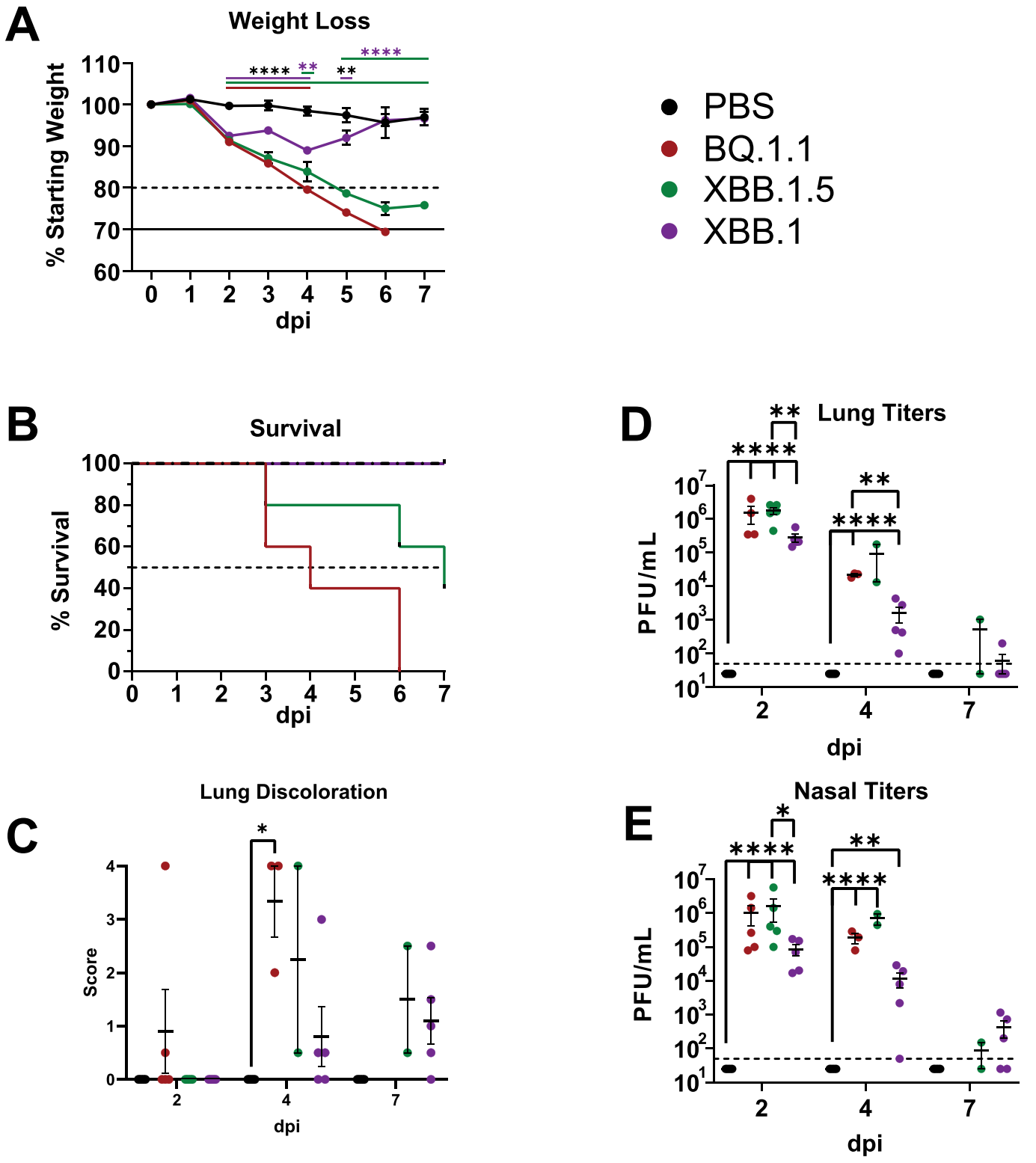

Fig. 1. Divergent Disease Phenotypes Observed Between Evolved Omicron Sublineages. Mouse adapted infectious clones of Omicron sublineage variants were used to infect cohorts of fifteen 11 – 12 months old female BALB/c mice. The resulting disease phenotypes were monitored for seven days. **(A)** Percent weight lost from starting weight is shown as group mean with standard error of the mean for each day of the study. Dashed horizontal line indicates 20 % of starting weight loss. Solid horizontal line represents 30 % weight loss and endpoint criteria for humane euthanasia due to weight loss. **(B)** Group survival of the cohort of five mice selected to be sacrificed at 7-dpi is shown. Dashed line represents 50 % mortality. **(C)** Qualitative gross lung discoloration scores, representing discoloration of lung lobes at the time of harvest, are shown. **(D & E)** Lung and nasal tissue titers as determined by plaque assay are shown as log10 transformed values. Dashed lines represent the assay limit of detection. Error bars represent standard error of the mean. Statistical significance was determined by two-way ANOVA with Tukey's multiple comparison test for weight loss, Kruskal-Wallis non-parametric test with Dunn's correction lung discoloration, and one-way ANOVA with Tukey's multiple comparison test for lung and nasal titers. * = $p < 0.05$, ** = $p < 0.01$, **** = $p < 0.0001$. Horizontal bars in Fig. A indicate the virus and asterisk color represents virus compared to.

= 0.005)(Fig. 1**D**). Similarly, XBB.1 MA replication was also reduced by more than a log in the nose, achieving maximal titers of only 8.67×10^4 PFU/mL (SEM = 3.27×10^4, $N = 5$)(Fig. 1**E**).

3.3.5. *Lung histology*

Histopathology was evident in all the lung tissue sections from mice that were infected with the Omicron variants on 2-, 4- and 7-dpi (6-dpi for BQ.1.1). In contrast, saline-instilled mock (control) mice had little if any discernable lung histopathology at any time post instillation. Virus-induced lung lesions were most prominent in mice that received the BQ.1.1 and XBB.1.5 variants, with similar but less severe lesions in XBB.1. For example, virus infected mice had acute/subacute

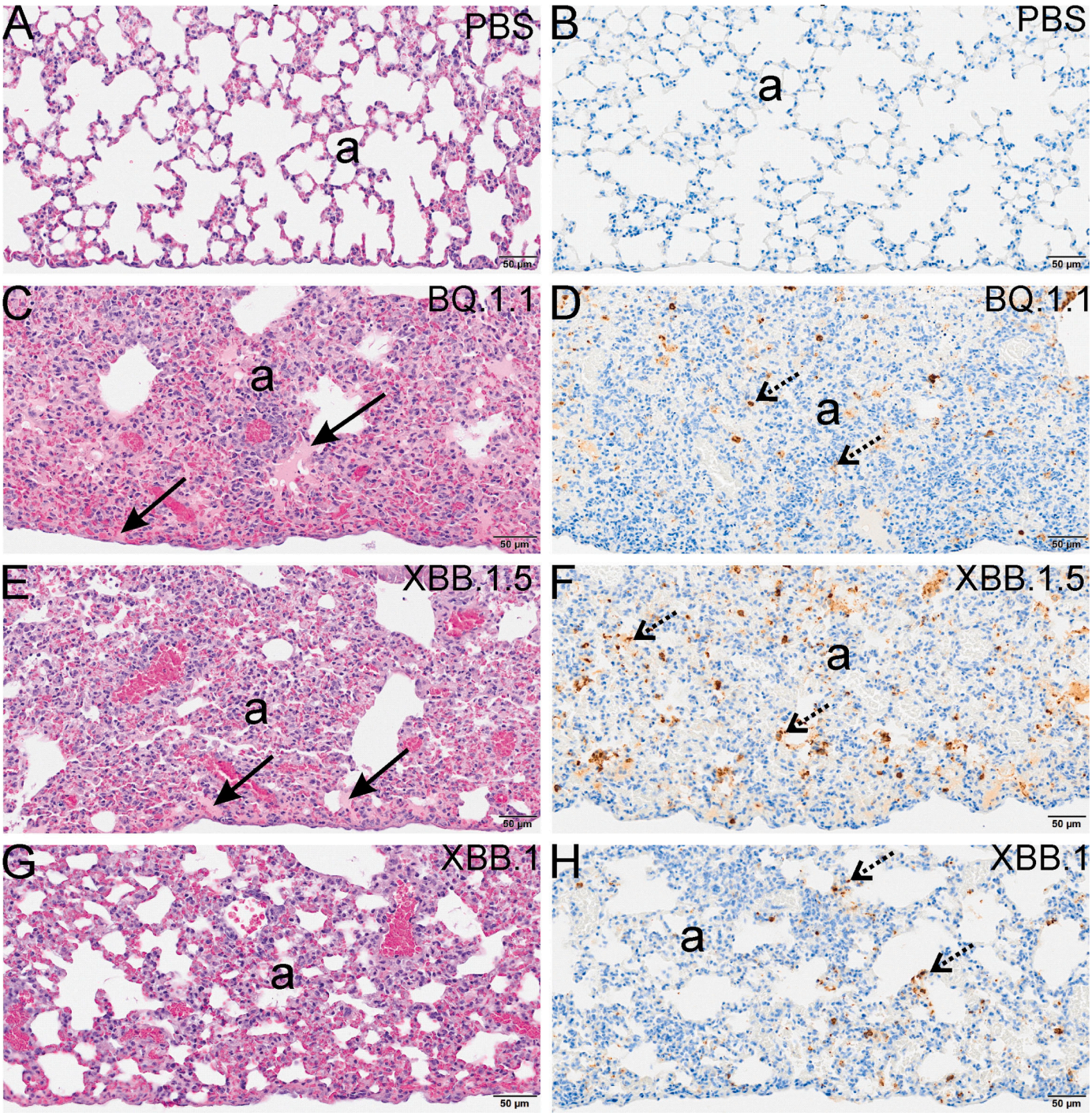

Fig. 2. BQ.1.1 MA and XBB.1.5 MA Display Increased SARS2 Nucleocapsid Protein Throughout Airway as Compared to XBB.1 at 2 Days Post Infection. Representative light photomicrographs of alveolar lung tissue from mice instilled with Omicron variants–BQ.1.1 MA **(C, D)**, XBB.1.5 MA **(E, F)**, XBB.1 MA **(G, H)**, or mock vehicle alone (phosphate buffered saline, PBS) **(A, B)**, and taken for microscopic examination at 2 days post-instillation (dpi). **(A, C, E, G)** Tissue sections were histochemically stained with hematoxylin and eosin (H&E). **(B, D, F, H)** Sections were also stained immunohistochemically for viral protein (solid arrows) and counterstained with hematoxylin. **(A, B)** No histopathology or viral protein in mock control lungs. **(C, D)** Congested alveolar septa, alveolitis, peri-vascular accumulation of inflammatory cells, subpleural amorphous proteinaceous fluid (solid arrows in C) and widely scattered viral proteins (solid arrows in D). **(E, F)** Similar histopathology and immunohistochemistry as in C and D, respectively. **(G, H)** Similar but slightly less severe histopathology as in C and E. Less immunohistochemical staining for viral protein **(H)** as compared D and F. a, alveolar parenchyma. Scale bar equals 50 µm.

bronchopneumonia characterized by lung lesions consisting of alveolitis and bronchiolitis with mixed inflammatory cell infiltrates of neutrophils and mononuclear leukocytes (monocytes and lymphoid cells), thickened and congested alveolar septa, loss of alveolar air spaces, varying amounts of amorphous proteinaceous fluid in alveolar air spaces (mainly in subpleural regions), increased numbers of alveolar macrophages/monocytes, and peri-vascular/-bronchiolar inflammatory cell accumulation. Light photomicrographs in Figs. 2, 3, and 4 illustrate lung histopathology at the various time points after infection, and the immunohistochemical staining to spatially identify cellular and extracellular viral protein scattered throughout the lung tissue.

At 2-dpi, occasional scattered foci of cellular proteinaceous or nuclear debris were present along alveolar septa and commonly associated with stained viral protein and acute inflammatory lesions **(**Fig. 2**C** & **E solid arrows)**. Immunohistochemically stained viral protein was principally located in type 2 alveolar epithelial cells with rare staining in bronchiolar epithelium and alveolar macrophages **(**Fig. 2**B, D, F** & **H stippled arrows)**. Reduced amounts of stained viral protein were found in lung tissue from XBB.1 infected mice as compared to animals infected with the two other Omicron S variants.

By 4-dpi, less proteinaceous fluid was present in the alveolar airspaces of XBB.1 infected mice, which also had slightly less congestion and inflammation in the alveolar parenchyma as compared to the lungs taken at this same time point from the other variant infected mice **(**Fig. 3**A, C, E,** & **G solid arrows)**. In addition, stained viral protein was diminished in lung tissue sections from all virally infected mice with little to no immunohistochemical staining in the lungs of XBB.1 animals **(**Fig. 3**B, D, F,** & **H solid arrows)**. More extracellular viral protein and alveolar macrophages containing cytoplasmic viral protein were present in the lung at 4-dpi as compared to 2-dpi.

Initial alveolar repair of viral-induced injury was evident at 6-dpi for BQ.1.1 and at 7-dpi for XBB.1 and XBB.1.5 with focal areas of type 2 alveolar epithelial cell hyperplasia and hypertrophy, as well as some bronchiolar epithelial hyperplasia/hypertrophy, in all variant-instilled mice (data for BQ.1.1 is a mouse that was sacrificed due to humane endpoint at 6-dpi). XBB.1 infected mice had the most reparative type 2 alveolar epithelial cell hyperplasia **(**Fig. 4**G stippled arrow)**, as well as no accumulation of proteinaceous fluid in alveolar air spaces, the latter lesion being still present in lungs of the BQ.1.1 and XBB.1.5 mice **(**Fig. 4**C** & **E Solid arrows)**. At this post-instillation time point, immunohistochemically stained viral protein was minimal in the lungs of BQ.1.1 and XBB.1.5 mice and absent in the lung tissue of XBB.1 mice. Together, these data indicate a significantly reduced infection, clinical and pathologic disease phenotypes in XBB.1 mice, which differ from XBB.1.5 by a single amino acid change at position S F486.

3.4. Lung dysfunction

To determine the impact of viral infection on lung function, a replicate study consisting of cohorts of five 10 – 12 month of female BALB/c mice that were inoculated with 50 μL of either 10^5 PFU of BQ.1.1 MA, XBB.1.5 MA, or XBB.1 MA; or 50 μL of 10^4 PFU MA10; and PBS controls was employed. Mice were evaluated daily for weight loss, mortality, and lung dysfunction. At 7 dpi all surviving mice were harvested for quantification of lung discoloration and tissue titers. A log reduced quantity of MA10 was utilized as the virus is highly virulent at a dose of 10^4 PFU and infection elicits severe disease phenotypes that are similar to those observed in BQ.1.1 and XBB.1.5 infected aged animals. Mice were monitored daily by whole-body plethysmography for the effect of infection on the ratio of time to peak expiratory follow (PEF) relative to the total expiratory time (Rpef), airway resistance by enhanced pause (Penh), and mid-tidal expiratory flow (EF50) as previously described (Leist et al., 2020; Menachery et al., 2015). The Rpef and PenH measurements reflect bronchoconstriction and airway resistance phenotypes. Over the course of seven days, mice were also observed for weight loss and mortality. After infection, PenH values peaked at 2-dpi, representing the most serious phase of bronchoconstriction were significantly elevated as compared to mock infected controls, regardless of virus strain ($p < 0.01$). PenH maximal values were highest after MA10 and BQ.1.1 MA infections, leading to group mean averages of almost 5 at day 2 **(**Fig. 5**A)**. Values for all groups trended towards recovery starting on 3-dpi, although both XBB.1 and XBB.1.5 MA groups remained somewhat elevated, when compared to mock controls at 7-dpi. All viruses maintained significantly elevated PenH values through day 4, after which XBB.1 MA mice values returned to baseline before beginning to trend upwards at 7-dpi. Measurements at 5-dpi were the one timepoint where significant differences between XBB.1 and XBB.1.5 were observed (green bar with purple asterisks, $p < 0.01$). XBB.1.5 MA infected animals maintained significantly elevated values when compared to mock controls throughout the course of the experiment (green bars with black asterisks). Of the four viruses, XBB.1 MA produced the lowest deviation from the mock PBS control mice even though it displayed a marked increase in lung dysfunction, with significant differences from PBS control mice noted at 2- and 4-dpi (purple bar with black asterisks, $p < 0.01$).

Rpef values were maximally altered after 2-dpi for all infected mice, and this phenotype remained relatively equivalent across all infection groups except the mock controls ($p < 0.0001$) **(**Fig. 5**B)**. Infected cohorts trended to recovery and reflected mock control baseline values after 3-dpi, except for XBB.1.5 which demonstrated a delayed recovery phenotype. Finally, EF50 values demonstrated a spike at 2-dpi for all groups **(**Fig. 5**C)**. As with PenH data, Rpef values for XBB.1.5 remained at significantly increased levels through day 4–7, when compared to both control and XBB.1 MA cohorts (green bar with black and purple asterisks, $p < 0.0001$).

In addition to lung function, weight loss was severe and continued to progress without recovery for the BQ.1.1 MA group **(**Fig. 5**D, red line)** and was comparable to that observed for the mice infected with 10^4 PFU of MA10 **(**Fig. 5**D, orange line)**. Similarly, XBB.1.5 MA displayed a rapid decrease in group average weight to ~75 % of their starting values, while XBB.1 MA mice only lost ~10 % of their starting weights and trended towards recovery once reaching their maximal loss at 3-dpi. Following day 3, XBB.1.5 MA cohort group mean weights were significantly reduced when compared to both PBS and XBB.1 cohorts (green bar with black and purple asterisks, $p < 0.0001$). The parental MA10 strain was highly pathogenic, despite the 10-fold lower inoculating dose, supporting the hypothesis that Omicron-related S genes were less pathogenic.

Analysis of group survival once again indicated severe mortality induced by infection from BQ.1.1 MA, with all group members succumbing by 5-dpi **(**Fig. 5**E)**. This was comparable to the mortality observed for MA10 infected mice as all mice from that cohort had perished by 6-dpi. Whereas in the first study 3 of 5 mice from the XBB.1.5 MA cohort perished, only 1 of 4 died in this cohort (one mouse was lost following anesthesia for infection). In contrast, 1 of 5 mice from the XBB.1 MA group perished during the study, indicating that while rare, occasionally animals will experience a lethal infectious disease course outcome. In concordance with weight loss data, severe gross lung discoloration was observed in the mice that survived XBB.1.5 MA challenge at 7-dpi, while discoloration was absent for the XBB.1 mice ($p < 0.0001$)**(**Fig. 5**F)**. Similarly, elevated lung titers above the limit of detection were noted for 2 of the 3 surviving XBB.1.5 mice at 7-dpi, while only 2 of 4 mice infected with XBB.1 had detectable titers **(**Fig. 5**G)**.

4. Discussion

SARS-CoV-2 has caused considerable morbidity and mortality in human populations since its emergence in China in the late fall of 2019. Like other human coronaviruses which are endemic in human populations, SARS-CoV-2 continues to evolve rapidly, leading to repeat infections throughout life. The ancestral human SARS-CoV-2 Wuhan strain

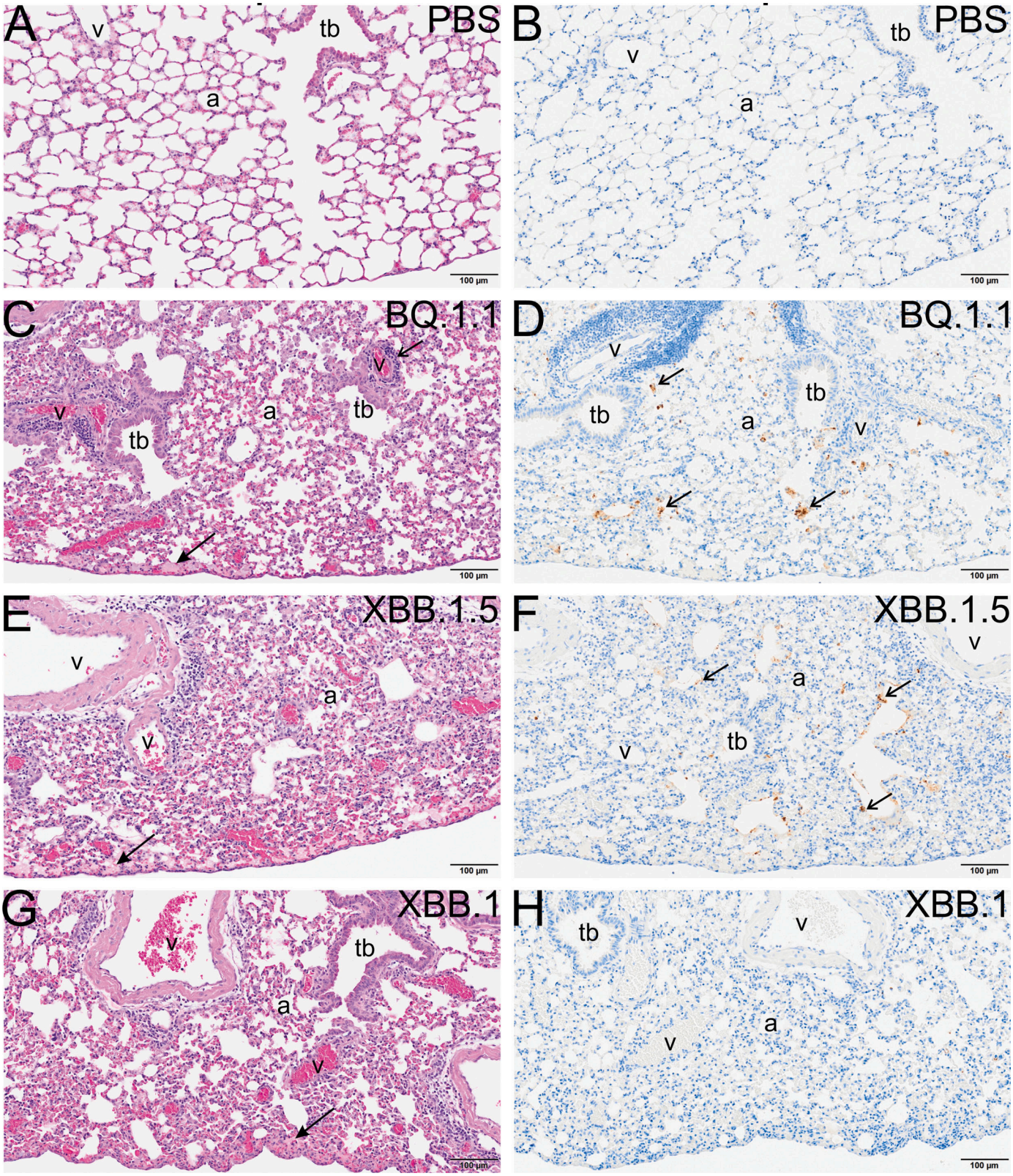

Fig. 3. Increased Proteinaceous Debris and Airway Inflammation Observed in XBB.1 Infected Mice at 4 Days Post Infection compared to BQ.1.1 MA and XBB.1.5 MA. Representative light photomicrographs of alveolar lung tissue from mice instilled with Omicron variants–BQ.1.1 MA **(C, D)**, XBB.1.5 MA **(E, F)**, XBB.1 MA **(G, H)**, or mock vehicle alone (phosphate buffered saline, PBS) **(A, B)**, and taken for microscopic examination at 4 days post-instillation (dpi). **(A, C, E, G)** Tissue sections were histochemically stained with hematoxylin and eosin (H&E). **(B, D, F, H)** Sections were also immunohistochemically stained for viral protein (solid arrows) and counterstained with hematoxylin. **(A, B)** No histopathology or viral protein in mock control lungs. **(C, D)** Congested alveolar septa, alveolitis, peri-vascular/-bronchiolar accumulation of inflammatory cells, subpleural amorphous proteinaceous fluid (solid arrow in C) and a few widely scattered viral proteins (solid arrows in D). **(E, F)** Similar histopathology and immunohistochemistry as in C and D, respectively. **(G, H)** Similar but slightly less severe histopathology as in C and E. No immunohistochemical staining for viral protein **(H)**. tb, terminal bronchiole; v, blood vessel; a, alveolar parenchyma. Scale bar equals 100 µm.

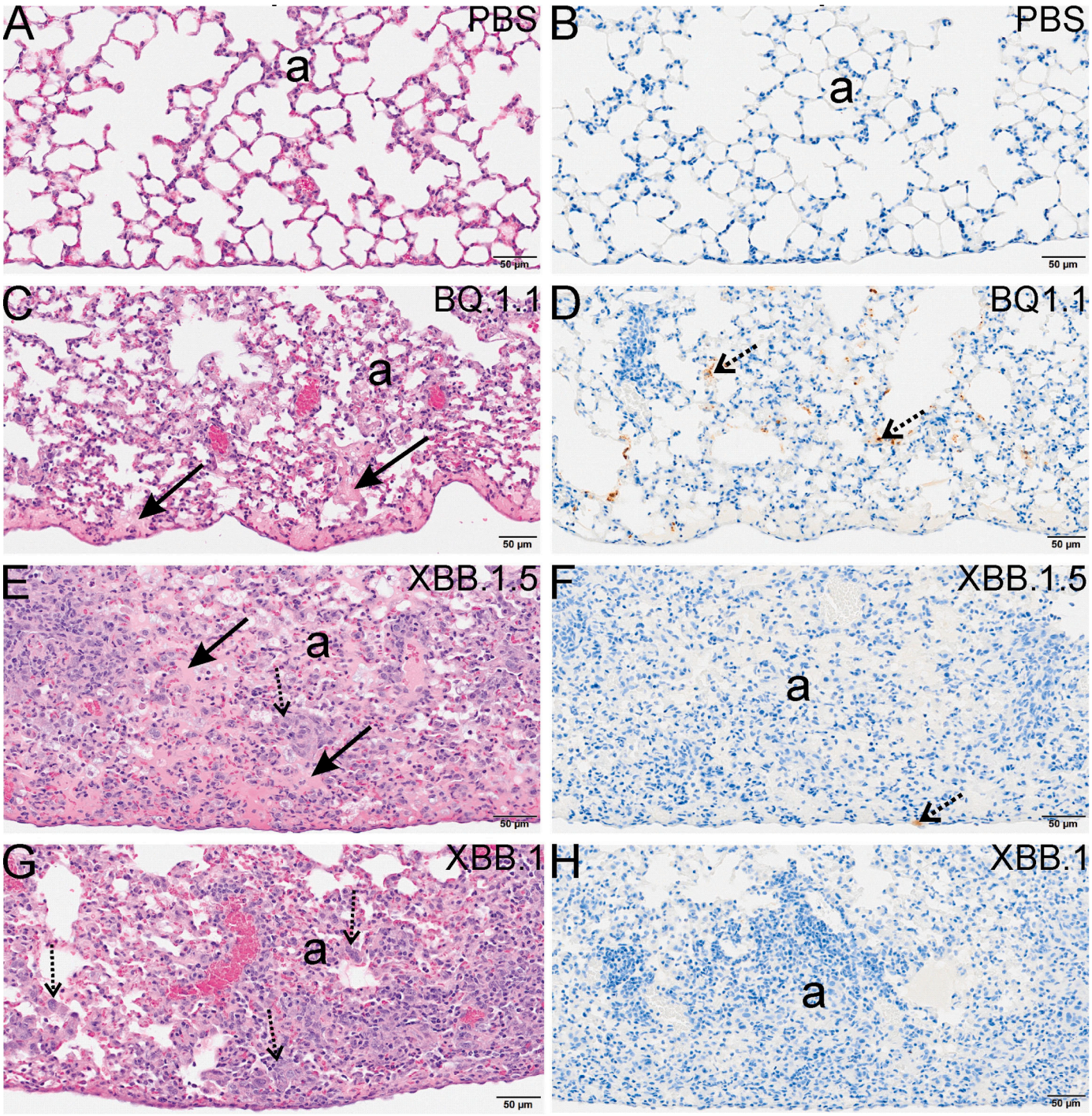

Fig. 4. XBB.1 Infected Mice Display Increased Reparative Type 2 Alveolar Epithelial Cell Hyperplasia. Representative light photomicrographs of alveolar lung tissue (a) from mice instilled with Omicron variants–BQ.1.1 MA **(C, D)**, XBB.1.5 MA **(E, F)**, XBB.1 MA **(G, H)**, or mock vehicle alone (phosphate buffered saline, PBS) **(A, B)**, and taken for microscopic examination at 7 days post-instillation (dpi)(6-dpi for BQ.1.1 MA). **(A, C, E, G)** Tissue sections were histochemically stained with hematoxylin and eosin (H&E). **(B, D, F, H)** Sections were also immunohistochemically stained for viral protein (stippled arrows) and counterstained with hematoxylin. **(A, B)** No histopathology or viral protein in mock control lungs. **(C, D)** Congested alveolar septa, alveolitis, subpleural amorphous proteinaceous fluid (solid arrows in C) and a few widely scattered viral proteins (stippled arrows in D). **(E, F)** Congested alveolar septa, alveolitis, subpleural amorphous proteinaceous fluid (solid arrows in C) and a solitary small focus of viral protein (stippled arrows in F). **(G, H)** Congested alveolar septa with areas of type 2 alveolar epithelial cell hyperplasia/hypertrophy (stippled arrows in G), no proteinaceous fluid in alveolar air spaces **(G)**, and no immunohistochemical staining for viral protein **(H)**. a, alveolar parenchyma. Scale bar equals 50 µm.

rapidly adapted to human populations by evolving mutations in the S glycoprotein that enhanced hACE2 interactions, infectivity and transmission. As herd immunity increased in human populations due to natural infection and vaccination, new evolutionary patterns emerged that were associated with mutations that enhanced escape from circulating neutralizing antibodies (Zamorano Cuervo and Grandvaux, 2020; Tao et al., 2021; Zahradnik et al., 2021; Roemer et al., 2023; Corman et al., 2018; Eckerle et al., 2010; Eguia et al., 2021). In particular additional S mutations were rapidly selected that altered antigenic properties in the RBD, NTD and in S2, leading to enhanced resistance to

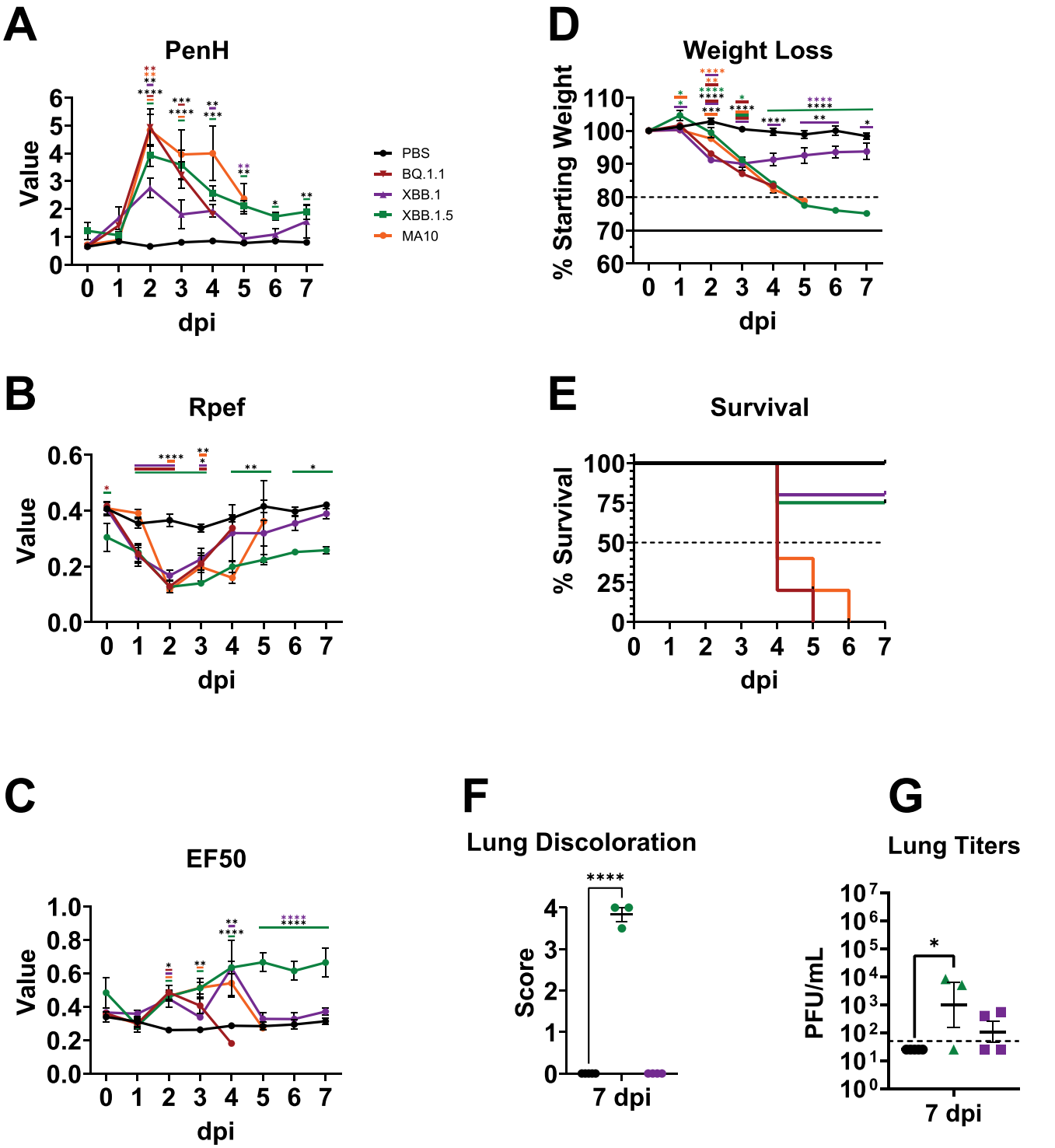

Fig. 5. Concordance between Lung Dysfunction and Gross Pathologic Disease. Cohorts of five mice per infectious clone Omicron sublineage variant were used to assess infection impact on lung function dynamics. Comparator control arms include a mock infected group, as well as the ancestral MA10 strain virus. **(A – C)** Pulmonary function and the resulting impacts from infection were monitored daily by whole-body plethysmography. Rpef, PenH, and EF50 were recorded. Group means are shown with standard error of the mean shown. **(D)** Percent weight lost from starting weight is shown as group mean with standard error of the mean for each day of the study. Dashed line indicates 20 % of starting weight loss. Solid line represents humane euthanasia endpoint criteria for weight loss. **(E)** Impacts of infection on survival were tracked over the course of the study. Dashed line represents 50 % mortality. **(F)** Cohorts with surviving members at 7-dpi were sacrificed and qualitative gross lung discoloration scores, representing discoloration of lung lobes at the time of harvest, were recorded. Error bars represent standard error of the mean. **(G)** Lung tissue titers as determined by plaque assay are shown as log10 transformed values. Dashed lines represent the assay limit of detection. Error bars represent standard error of the mean. Statistical significance was determined by two-way ANOVA with Tukey's multiple comparison test for weight loss PenH, Rpef, and EF50 values; Kruskal-Wallis non-parametric test with Dunn's correction lung discoloration; and one-way ANOVA with Tukey's multiple comparison test for tissue titers. * = $p < 0.05$, ** = $p < 0.01$, *** = $p < 0.001$ **** = $p < 0.0001$. The horizontal bars in panels A–D indicate the virus and asterisk color represents virus compared to.

commercially available therapeutic monoclonal antibodies and vaccines (Li et al., 2020; Carabelli et al., 2023; Zabidi et al., 2023). While non-vaccinated individuals experience more severe disease and increased mortality rates as compared with vaccinated populations, the emergence of new VOC continue to cause significant human disease and high transmission rates, even amongst vaccinated populations or patients infected by prior variants (Keyel et al., 2022; Regenhardt et al., 2023; Briciu et al., 2023; Pulliam et al., 2022). The development of small animal models that more accurately reflect pulmonary centered disease phenotypes without incidence of neuroinvasion, as well as the occasional severe disease phenotypes seen in some human populations, provide important opportunities for studying pathogenic mechanisms and countermeasure performance (Kumari et al., 2021; Golden et al., 2020; Winkler et al., 2020; Zheng et al., 2021). As wildtype Omicron strains are oftentimes highly attenuated in rodent models, these reagents provide new opportunities to study acute and chronic pulmonary centered disease states seen in human patients (Leist et al., 2020; Hou et al., 2020; Halfmann et al., 2022; Liu et al., 2022; Shuai et al., 2023; Kumari et al., 2021; Golden et al., 2020). Additionally, the utility of the nLuc expressing constructs enables assessment of antibody and sera capacity to neutralize virus in a moderate throughput live virus assay with a straightforward read-out (Garrido et al., 2021; Feng et al., 2023; Martinez et al., 2023; Mallory et al., 2023; Hou et al., 2020).

A variety of S glycoprotein mutations are associated with specific changes in ACE2 receptor usage, entry efficiency, transmissibility in hamster models, viral pathogenesis and escape from immunotherapeutic countermeasures (Wang et al., 2023; Liu et al., 2022; Escalera et al., 2022; Harvey et al., 2021; Hirabara et al., 2021; Chu and Yuen, 2022). Mutations at position 486 represent a frequent hotspot for change amongst the most recently emerging Omicron lineage variants. In fact, the F486 S residue had remained remarkably stable prior to the emergence of Omicron BA.5 (Zhang et al., 2023). Amongst the Omicron variants studied here, mutations at this site include F486V (BQ.1.1), F486S (XBB.1), and F486P (XBB.1.5) (Ao et al., 2023; Tamura et al., 2023; Chakraborty et al., 2023). S glycoprotein position F486 is a known residue that influences S binding to position 83 (Y or P) in the human and mouse angiotensin-converting enzyme 2 (hACE2, mACE2) (Pach et al., 2021; Wan et al., 2020; Adams et al., 2021; Ni et al., 2023; Huang et al., 2020). Previous studies have also identified significant differences in hACE2 receptor affinity between XBB.1 and XBB.1.5 suggesting that a similar effect may be at play with these variants regarding mACE2 affinity and binding (Yue et al., 2023; Uriu et al., 2023). As such, the elevated disease phenotypes observed in BQ.1.1 MA and XBB.1.5 MA infected mice may reflect the beneficial phenotypes associated with receptor binding and entry favorability provided by the presence of the F486P/V mutations, but that is diminished in the presence of the F486S mutation seen in XBB.1. In fact, among the three variants tested here, serine for XBB.1 is the only amino acid with a polar side chain whereas the others retain hydrophobic side chains at S position F486. In fact, XBB.1 MA and XBB.1.5 MA differ at this single residue, providing strong support for the hypothesis that the divergence in measured disease metrics seen between XBB.1 and XBB.1.5 MA relates specifically to this position. Although speculative and more complex given the different numbers of S gene mutations, it seems likely that this residue also influences disease phenotypes seen in BQ.1.1 infected animals **(**Figs. 1–5**)**.

When compared to our ancestral MA10 virus, a log reduced dose of MA10 (10^4 PFU) was sufficient to elicit comparable disease metrics to BQ.1.1 MA and to an extent XBB.1.5 MA infected with a 10-fold higher dose. In contrast, mice infected with 10^5 PFU of XBB.1 MA displayed mild disease with more rapid recovery towards initial baseline, than the other viruses. As Leist et al. (2020) previously identified with the WA-1 isolate derived MA10, infectious dose exacerbated disease outcomes regardless of mouse age. Consequently, reduced doses of the Omicron variants are anticipated to reduce pathogenic disease burden and death, more reflective of outcomes commonly observed among human patients. At its peak, Omicron BA.1 infections were causing millions of infections resulting in over 4000 deaths/day in the US. As the goal of this research was to develop models whereby clear disease metrics could be observed and interventions could be evaluated, the mortality induced by high dose infection is more reflective of human pulmonary disease, with the acute phase of pulmonary disease marked by lung inflammation and lung dysfunction, and with the elderly most at risk for severe infection and disease complications (Fericean et al., 2023).

Clinical and virologic disease metrics were not only clearly reduced in XBB.1 infection as compared to XBB.1.5 and BQ.1.1 infections, but histopathological evaluation of tissues from mice sacrificed at 2-, 4-, and 7-dpi (6-dpi for BQ.1.1) further supported these findings by demonstrating reduced viral nucleocapsid staining for XBB.1 infected mice when compared to BQ.1.1 and XBB.1.5, with expedited clearance. Additionally, XBB.1 infected mice had reduced proteinaceous debris, congestion, and inflammation when compared to the other Omicron variants **(**Figs. 2–4**).** The increased and sustained inflammation exhibited within the lungs of infected mice as observed by histopathological examination coincides with data on attenuated respiratory function and again is consistent with the presence of the F486S mutation at position F486 in the XBB.1 S glycoprotein **(**Fig. 5**A–C).**

BQ.1.1 displayed similar disease trajectories for PenH, Rpef, weight loss, and survival as MA10 in a side-by side experiment, although recovery towards mock infected controls was noted earlier for EF50 values **(**Fig. 5**A–E).** In comparison, XBB.1.5 infected cohorts also showed similar disease trajectories as MA10 and BQ.1.1, although they did not experience a return to baseline values when lung dysfunction was assessed by PenH, Rpef, and EF50 and overall mortality was diminished. In contrast, XBB.1 mice achieved a maximal weight loss of approximately 10 % with decreased impacts on PenH when compared to all the other viruses studied **(**Fig 5 **A** & **D)**.

Using a live-virus nLuc neutralization assays and sera from mice vaccinated with an alum adjuvanted Wuhan S2P protein vaccine, we observed a significance decrease in neutralizing antibody titer against the three Omicron nLuc viruses as compared to SARS-CoV-2 D614G **(Supplemental Fig. 2C)**. Antibodies retained the most activity against BQ.1.1 nLuc, reflecting the reduced numbers of amino acid changes as compared with XBB.1 and XBB.1.5. Further reductions were observed with XBB.1 and XBB.1.5 with only 3 and 2 serum samples neutralizing above the limit of detection, respectively. Interestingly, of the twenty serum samples tested, some failed to neutralize D614G, indicating variability in vaccination response among the vaccinated BALB/c mice. Of note, two of the mice that failed to neutralize D614G showed neutralizing activity against the variants. From one mouse, serum was able to neutralize BQ.1.1 ($ID_{50} = 65$), while the other serum sample was capable of neutralizing both BQ.1.1 ($ID_{50} = 564$), as well as XBB.1 ($ID_{50} = 74$). Neither of these two samples elicited neutralizing activity against XBB.1.5.

In conclusion, our findings presented here reflect the amenability of SARS-CoV-2 VOCs to be studied in standard BALB/c mice, abrogating the need to rely on transgenic mice that have known limitations in modeling a pulmonary specific acute phase disease (Kumari et al., 2021; Golden et al., 2020). Pathogenesis is easily tracked through multiple metrics including weight loss, lung function, and mortality, enabling amenability to the study of monoclonal antibodies, therapeutics, and vaccine approaches. Coupled with the nLuc expressing recombinant viruses for moderate throughput neutralization assays, this panel of Omicron variants provides powerful tools to elucidate the emerging landscape of Omicron sublineage viruses. As BA.2.86, the most extraordinarily mutated Omicron subvariant based on the number of S gene mutations while retaining the F486P mutation, further assessment of the impact of proline mutation at the F486 site may provide valuable information regarding receptor binding affinity, usage, and amenability to using non-human ACE2 receptors.

4.1. Authorship statement

The data included has not been published elsewhere, and the listed authors are all support of the publication of this manuscript. Contributions to the acquisition of data and formulation of the manuscript are as follows:

CRediT authorship contribution statement

John M. Powers: Project administration, Conceptualization, Formal analysis, Investigation, Methodology, Resources, Validation, Visualization, Writing – original draft, Writing – review & editing. **Sarah R. Leist:** Investigation, Writing – original draft, Writing – review & editing. **Michael L. Mallory:** Data curation, Formal analysis, Investigation, Validation. **Boyd L. Yount:** Methodology, Resources. **Kendra L. Gully:** Investigation, Resources. **Mark R. Zweigart:** Resources. **Alexis B. Bailey:** Resources. **Timothy P. Sheahan:** Formal analysis, Investigation, Writing – original draft, Writing – review & editing. **Jack R. Harkema:** Formal analysis, Resources, Visualization, Writing – review & editing. **Ralph S. Baric:** Funding acquisition, Project administration, Supervision, Writing – original draft, Writing – review & editing.

Declaration of competing interest

The authors declare the following financial interests/personal relationships which may be considered as potential competing interests:

R.S.B and S.R.L hold a patent for the SARS-CoV-2 MA10 virus, patent number (US 11,225,508 B1, "Mouse-adapted SARS-CoV-2 Viruses And Methods Of Use Thereof").

Data availability

Data will be made available on request.

Acknowledgments

We thank N.J. Thornburg at the CDC for providing us with the SARS-CoV-2 clinical isolate WA1 strain. The research was supported by research grants AI158571, AI110700 and AI167966 to RSB. The UNC Animal Histopathology & Laboratory Medicine Core is supported in part by an NCI Center Core Support Grant (P30CA016086) to the UNC Lineberger Comprehensive Cancer Center. Adrian Creanga and Barney Graham from the Vaccine Research Center (NIAID, Bethesda, MD) for a gift of Vero E6 TMPRSS2/ACE2 overexpressing cells. Authors also thank R.P. Lewandowski at Michigan State University for digitally scanning the histologic whole glass slides.

Supplementary materials

Supplementary material associated with this article can be found, in the online version, at doi:10.1016/j.virusres.2024.199319.

References

Adams, L.E., Dinnon 3rd, K.H., Hou, Y.J., Sheahan, T.P., Heise, M.T., Baric, R.S., 2021. Critical ACE2 determinants of SARS-CoV-2 and group 2B coronavirus infection and replication. mBio 12 (2). https://doi.org/10.1128/mBio.03149-20.

Ao, D., He, X., Hong, W., Wei, X., 2023. The rapid rise of SARS-CoV-2 Omicron subvariants with immune evasion properties: XBB.1.5 and BQ.1.1 subvariants. MedComm 4 (2), e239. https://doi.org/10.1002/mco2.239 (2020)Epub 20230315PubMed PMID: 36938325; PubMed Central PMCID: PMCPMC10015854.

Briciu, V., Topan, A., Calin, M., Dobrota, R., Leucuta, D.C., Lupse, M., 2023. Comparison of COVID-19 severity in vaccinated and unvaccinated patients during the delta and Omicron wave of the pandemic in a romanian tertiary infectious diseases hospital. Healthcare 11 (3). https://doi.org/10.3390/healthcare11030373 (Basel)Epub 20230128PubMed PMID: 36766946; PubMed Central PMCID: PMCPMC9914916.

Carabelli, A.M., Peacock, T.P., Thorne, L.G., Harvey, W.T., Hughes, J., Consortium, C.G. U., et al., 2023. SARS-CoV-2 variant biology: immune escape, transmission and fitness. Nat. Rev. Microbiol. 21 (3), 162–177. https://doi.org/10.1038/s41579-022-00841-7. Epub 20230118PubMed PMID: 36653446; PubMed Central PMCID: PMCPMC9847462.

Chakraborty, C., Bhattacharya, M., Chopra, H., Islam, M.A., Saikumar, G., Dhama, K., 2023. The SARS-CoV-2 Omicron recombinant subvariants XBB, XBB.1, and XBB.1.5 are expanding rapidly with unique mutations, antibody evasion, and immune escape properties - an alarming global threat of a surge in COVID-19 cases again? Int. J. Surg. 109 (4), 1041–1043. https://doi.org/10.1097/JS9.0000000000000246. Epub 20230401PubMed PMID: 36917125; PubMed Central PMCID: PMCPMC10132296.

Chu, H., Yuen, K.Y., 2022. Pathogenicity of SARS-CoV-2 Omicron. Clin. Transl. Med. 12 (5), e880. https://doi.org/10.1002/ctm2.880. PubMed PMID: 35543251; PubMed Central PMCID: PMCPMC9092483.

Corman, V.M., Muth, D., Niemeyer, D., Drosten, C., 2018. Hosts and sources of endemic human coronaviruses. Adv. Virus Res. 100, 163–188. https://doi.org/10.1016/bs.aivir.2018.01.001. Epub 20180216PubMed PMID: 29551135; PubMed Central PMCID: PMCPMC7112090.

Dinnon 3rd, K.H., Leist, S.R., Schafer, A., Edwards, C.E., Martinez, D.R., Montgomery, S. A., et al., 2020. A mouse-adapted model of SARS-CoV-2 to test COVID-19 countermeasures. Nature 586 (7830), 560–566. https://doi.org/10.1038/s41586-020-2708-8. Epub 20200827PubMed PMID: 32854108; PubMed Central PMCID: PMCPMC8034761.

Eckerle, L.D., Becker, M.M., Halpin, R.A., Li, K., Venter, E., Lu, X., et al., 2010. Infidelity of SARS-CoV Nsp14-exonuclease mutant virus replication is revealed by complete genome sequencing. PLoS Pathog. 6 (5), e1000896 https://doi.org/10.1371/journal.ppat.1000896. Epub 20100506PubMed PMID: 20463816; PubMed Central PMCID: PMCPMC2865531.

Eguia, R.T., Crawford, K.H.D., Stevens-Ayers, T., Kelnhofer-Millevolte, L., Greninger, A. L., Englund, J.A., et al., 2021. A human coronavirus evolves antigenically to escape antibody immunity. PLoS Pathog. 17 (4), e1009453 https://doi.org/10.1371/journal.ppat.1009453. Epub 20210408PubMed PMID: 33831132; PubMed Central PMCID: PMCPMC8031418.

Escalera, A., Gonzalez-Reiche, A.S., Aslam, S., Mena, I., Laporte, M., Pearl, R.L., et al., 2022. Mutations in SARS-CoV-2 variants of concern link to increased spike cleavage and virus transmission. Cell Host Microbe 30 (3), 373–387. https://doi.org/10.1016/j.chom.2022.01.006 e7. Epub 20220121PubMed PMID: 35150638; PubMed Central PMCID: PMCPMC8776496.

Feng, Y., Yuan, M., Powers, J.M., Hu, M., Munt, J.E., Arunachalam, P.S., et al., 2023b. Broadly neutralizing antibodies against sarbecoviruses generated by immunization of macaques with an AS03-adjuvanted COVID-19 vaccine. Sci. Transl. Med. 15 (695), eadg7404. https://doi.org/10.1126/scitranslmed.adg7404. Epub 20230510PubMed PMID: 37163615.

Feng, Y., Yuan, M., Powers, J.M., Hu, M., Munt, J.E., Arunachalam, P.S., et al., 2023a. Extremely Potent Pan-Sarbecovirus Neutralizing Antibodies Generated by Immunization of Macaques with an AS03-Adjuvanted Monovalent Subunit Vaccine Against SARS-CoV-2. bioRxiv. https://doi.org/10.1101/2023.01.19.524784. Epub 20230120PubMed PMID: 36711543; PubMed Central PMCID: PMCPMC9882348.

Fericean, R.M., Oancea, C., Reddyreddy, A.R., Rosca, O., Bratosin, F., Bloanca, V., et al., 2023. Outcomes of elderly patients hospitalized with the SARS-CoV-2 Omicron B.1.1.529 variant: a systematic review. Int. J. Environ Res. Public Health 20 (3). https://doi.org/10.3390/ijerph20032150. Epub 20230125PubMed PMID: 36767517; PubMed Central PMCID: PMCPMC9915911.

2nd Garrido, C., Curtis, A.D., Dennis, M., Pathak, S.H., Gao, H., Montefiori, D., et al., 2021. SARS-CoV-2 vaccines elicit durable immune responses in infant rhesus macaques. Sci. Immunol. 6 (60). https://doi.org/10.1126/sciimmunol.abj3684. PubMed PMID: 34131024; PubMed Central PMCID: PMCPMC8774290.

Gili, R., Burioni, R., 2023. SARS-CoV-2 before and after Omicron: two different viruses and two different diseases? J. Transl. Med. 21 (1), 251. https://doi.org/10.1186/s12967-023-04095-6. Epub 20230410PubMed PMID: 37038133; PubMed Central PMCID: PMCPMC10088248.

Golden, J.W., Cline, C.R., Zeng, X., Garrison, A.R., Carey, B.D., Mucker, E.M., et al., 2020. Human angiotensin-converting enzyme 2 transgenic mice infected with SARS-CoV-2 develop severe and fatal respiratory disease. JCI Insight 5 (19). https://doi.org/10.1172/jci.insight.142032. Epub 20201002PubMed PMID: 32841215; PubMed Central PMCID: PMCPMC7566707.

Greaney, A.J., Loes, A.N., Crawford, K.H.D., Starr, T.N., Malone, K.D., Chu, H.Y., et al., 2021. Comprehensive mapping of mutations in the SARS-CoV-2 receptor-binding domain that affect recognition by polyclonal human plasma antibodies. Cell Host Microbe 29 (3), 463–476. https://doi.org/10.1016/j.chom.2021.02.003 e6. Epub 20210208PubMed PMID: 33592168; PubMed Central PMCID: PMCPMC7869748.

Halfmann, P.J., Iida, S., Iwatsuki-Horimoto, K., Maemura, T., Kiso, M., Scheaffer, S.M., et al., 2022. SARS-CoV-2 Omicron virus causes attenuated disease in mice and hamsters. Nature 603 (7902), 687–692. https://doi.org/10.1038/s41586-022-04441-6. Epub 20220121PubMed PMID: 35062015; PubMed Central PMCID: PMCPMC8942849.

Harvey, W.T., Carabelli, A.M., Jackson, B., Gupta, R.K., Thomson, E.C., Harrison, E.M., et al., 2021. SARS-CoV-2 variants, spike mutations and immune escape. Nat. Rev. Microbiol. 19 (7), 409–424. https://doi.org/10.1038/s41579-021-00573-0. Epub 20210601PubMed PMID: 34075212; PubMed Central PMCID: PMCPMC8167834.

Hirabara, S.M., Serdan, T.D.A., Gorjao, R., Masi, L.N., Pithon-Curi, T.C., Covas, D.T., et al., 2021. SARS-COV-2 variants: differences and potential of immune evasion. Front. Cell Infect. Microbiol. 11, 781429 https://doi.org/10.3389/fcimb.2021.781429. Epub 20220118PubMed PMID: 35118007; PubMed Central PMCID: PMCPMC8805732.

Hoffmann, M., Kleine-Weber, H., Schroeder, S., Kruger, N., Herrler, T., Erichsen, S., et al., 2020. SARS-CoV-2 cell entry depends on ACE2 and TMPRSS2 and is blocked by a clinically proven protease inhibitor. Cell 181 (2), 271–280. https://doi.org/

10.1016/j.cell.2020.02.052 e8. Epub 20200305PubMed PMID: 32142651; PubMed Central PMCID: PMCPMC7102627.
Hou, Y.J., Chiba, S., Halfmann, P., Ehre, C., Kuroda, M., Dinnon, K.H., et al., 2020b. SARS-CoV-2 D614G variant exhibits efficient replication ex vivo and transmission *in vivo*. Science 370 (6523), 1464–1468. https://doi.org/10.1126/science.abe8499. Epub 20201112PubMed PMID: 33184236; PubMed Central PMCID: PMCPMC7775736.
Hou, Y.J., Okuda, K., Edwards, C.E., Martinez, D.R., Asakura, T., Dinnon, K.H., et al., 2020a. SARS-CoV-2 reverse genetics reveals a variable infection gradient in the respiratory tract. Cell 182 (2), 429–446. https://doi.org/10.1016/j.cell.2020.05.042 e14Epub 20200527PubMed PMID: 32526206; PubMed Central PMCID: PMCPMC7250779.
Huang, Y., Yang, C., Xu, X.F., Xu, W., Liu, S.W., 2020. Structural and functional properties of SARS-CoV-2 spike protein: potential antivirus drug development for COVID-19. Acta Pharmacol. Sin. 41 (9), 1141–1149. https://doi.org/10.1038/s41401-020-0485-4. Epub 20200803PubMed PMID: 32747721; PubMed Central PMCID: PMCPMC7396720.
Jungreis, I., Sealfon, R., Kellis, M., 2021. SARS-CoV-2 gene content and COVID-19 mutation impact by comparing 44 Sarbecovirus genomes. Nat. Commun. 12 (1), 2642. https://doi.org/10.1038/s41467-021-22905-7. Epub 20210511PubMed PMID: 33976134; PubMed Central PMCID: PMCPMC8113528.
Keyel, A.C., Russell, A., Plitnick, J., Rowlands, J.V., Lamson, D.M., Rosenberg, E., et al., 2022. SARS-CoV-2 vaccine breakthrough by Omicron and delta variants, New York, USA. Emerg. Infect. Dis. 28 (10), 1990–1998. https://doi.org/10.3201/eid2810.221058. Epub 20220901PubMed PMID: 36048774; PubMed Central PMCID: PMCPMC9514330.
Kim, D., Lee, J.Y., Yang, J.S., Kim, J.W., Kim, V.N., Chang, H., 2020. The architecture of SARS-CoV-2 transcriptome. Cell 181 (4), 914–921. https://doi.org/10.1016/j.cell.2020.04.011 e10. Epub 20200423PubMed PMID: 32330414; PubMed Central PMCID: PMCPMC7179501.
Kumari, P., Rothan, H.A., Natekar, J.P., Stone, S., Pathak, H., Strate, P.G., et al., 2021. Neuroinvasion and encephalitis following intranasal inoculation of SARS-CoV-2 in K18-hACE2 mice. Viruses 13 (1). https://doi.org/10.3390/v13010132. Epub 20210119PubMed PMID: 33477869; PubMed Central PMCID: PMCPMC7832889.
Lan, J., Ge, J., Yu, J., Shan, S., Zhou, H., Fan, S., et al., 2020. Structure of the SARS-CoV-2 spike receptor-binding domain bound to the ACE2 receptor. Nature 581 (7807), 215–220. https://doi.org/10.1038/s41586-020-2180-5. Epub 20200330PubMed PMID: 32225176.
Leist, S.R., Dinnon 3rd, K.H., Schafer, A., Tse, L.V., Okuda, K., Hou, Y.J., et al., 2020. A mouse-adapted SARS-CoV-2 induces acute lung injury and mortality in standard laboratory mice. Cell 183 (4), 1070–1085. https://doi.org/10.1016/j.cell.2020.09.050 e12. Epub 20200923PubMed PMID: 33031744; PubMed Central PMCID: PMCPMC7510428.
Letko, M., Marzi, A., Munster, V., 2020. Functional assessment of cell entry and receptor usage for SARS-CoV-2 and other lineage B betacoronaviruses. Nat Microbiol 5 (4), 562–569. https://doi.org/10.1038/s41564-020-0688-y. Epub 20200224PubMed PMID: 32094589; PubMed Central PMCID: PMCPMC7095430.
Li, Q., Wu, J., Nie, J., Zhang, L., Hao, H., Liu, S., et al., 2020. The impact of mutations in SARS-CoV-2 spike on viral infectivity and antigenicity. Cell 182 (5), 1284–1294. https://doi.org/10.1016/j.cell.2020.07.012 e9. Epub 20200717PubMed PMID: 32730807; PubMed Central PMCID: PMCPMC7366990.
Liu, S., Selvaraj, P., Sangare, K., Luan, B., Wang, T.T., 2022a. Spike protein-independent attenuation of SARS-CoV-2 Omicron variant in laboratory mice. Cell Rep. 40 (11), 111359 https://doi.org/10.1016/j.celrep.2022.111359. Epub 20220829PubMed PMID: 36075211; PubMed Central PMCID: PMCPMC9420700.
Liu, Y., Liu, J., Plante, K.S., Plante, J.A., Xie, X., Zhang, X., et al., 2022b. The N501Y spike substitution enhances SARS-CoV-2 infection and transmission. Nature 602 (7896), 294–299. https://doi.org/10.1038/s41586-021-04245-0. Epub 20211124PubMed PMID: 34818667; PubMed Central PMCID: PMCPMC8900207.
Mallory, M., Munt, J.E., Narowski, T.M., Castillo, I., Cuadra, E., Pisanic, N., et al., 2023. Longitudinal Analysis of Humoral and Cellular Immune Response Following SARS-CoV-2 Vaccination Supports Utilizing Point-Of-Care Tests to Enhance COVID-19 Booster Uptake. medRxiv. https://doi.org/10.1101/2023.04.03.23287498. Epub 20230404PubMed PMID: 37066219; PubMed Central PMCID: PMCPMC10104219.
Martinez, D.R., Schafer, A., Gavitt, T.D., Mallory, M.L., Lee, E., Catanzaro, N.J., et al., 2023. Vaccine-mediated protection against merbecovirus and sarbecovirus challenge in mice. Cell Rep., 113248 https://doi.org/10.1016/j.celrep.2023.113248. Epub 20231012PubMed PMID: 37858337.
Martinez, D.R., Schafer, A., Leist, S.R., Li, D., Gully, K., Yount, B., et al., 2021. Prevention and therapy of SARS-CoV-2 and the B.1.351 variant in mice. Cell Rep. 36 (4), 109450 https://doi.org/10.1016/j.celrep.2021.109450. Epub 20210710PubMed PMID: 34289384; PubMed Central PMCID: PMCPMC8270748.
Menachery, V.D., Gralinski, L.E., Baric, R.S., Ferris, M.T., 2015. New metrics for evaluating viral respiratory pathogenesis. PLoS One 10 (6), e0131451. https://doi.org/10.1371/journal.pone.0131451. Epub 20150626PubMed PMID: 26115403; PubMed Central PMCID: PMCPMC4482571.
Mykytyn, A.Z., Rosu, M.E., Kok, A., Rissmann, M., van Amerongen, G., Geurtsvankessel, C., et al., 2023. Antigenic mapping of emerging SARS-CoV-2 omicron variants BM.1.1.1, BQ.1.1, and XBB.1. Lancet Microbe 4 (5), e294–e2e5. https://doi.org/10.1016/S2666-5247(22)00384-6. Epub 20230116PubMed PMID: 36657480; PubMed Central PMCID: PMCPMC9842387.
Ni, D., Turelli, P., Beckert, B., Nazarov, S., Uchikawa, E., Myasnikov, A., et al., 2023. Cryo-EM structures and binding of mouse and human ACE2 to SARS-CoV-2 variants of concern indicate that mutations enabling immune escape could expand host range. PLoS Pathog. 19 (4), e1011206 https://doi.org/10.1371/journal.ppat.1011206. Epub 20230405PubMed PMID: 37018380; PubMed Central PMCID: PMCPMC10109501.
Pach, S., Nguyen, T.N., Trimpert, J., Kunec, D., Osterrieder, N., Wolber, G., 2021. ACE2-variants indicate potential SARS-CoV-2-susceptibility in animals: a molecular dynamics study. Mol. Inform. 40 (9), e2100031 https://doi.org/10.1002/minf.202100031. Epub 20210810PubMed PMID: 34378348; PubMed Central PMCID: PMCPMC8420607.
Pulliam, J.R.C., van Schalkwyk, C., Govender, N., von Gottberg, A., Cohen, C., Groome, M.J., et al., 2022. Increased risk of SARS-CoV-2 reinfection associated with emergence of Omicron in South Africa. Science 376 (6593), eabn4947. https://doi.org/10.1126/science.abn4947. Epub 20220506PubMed PMID: 35289632; PubMed Central PMCID: PMCPMC8995029.
Regenhardt, E., Kirsten, H., Weiss, M., Lubbert, C., Stehr, S.N., Remane, Y., et al., 2023. SARS-CoV-2 vaccine breakthrough infections of Omicron and delta variants in healthcare workers. Vaccines 11 (5). https://doi.org/10.3390/vaccines11050958 (Basel)Epub 20230507PubMed PMID: 37243062; PubMed Central PMCID: PMCPMC10220865.
Roemer, C., Sheward, D.J., Hisner, R., Gueli, F., Sakaguchi, H., Frohberg, N., et al., 2023. SARS-CoV-2 evolution in the Omicron era. Nat. Microbiol. https://doi.org/10.1038/s41564-023-01504-w. Epub 20231016PubMed PMID: 37845314.
Shuai, H., Chan, J.F., Hu, B., Chai, Y., Yoon, C., Liu, H., et al., 2023. The viral fitness and intrinsic pathogenicity of dominant SARS-CoV-2 Omicron sublineages BA.1, BA.2, and BA.5. eBioMedicine 95, 104753. https://doi.org/10.1016/j.ebiom.2023.104753. Epub 20230812PubMed PMID: 37579626; PubMed Central PMCID: PMCPMC10448076.
Silva Junior, J.V.J., Duraes-Carvalho, R., de Souza, J.R., Ramos Janini, L.M., Weiblen, R., Flores, E.F, 2023. Emergence of SARS-CoV-2 serotype(s): is it a matter of time? Virology 585, 78–81. https://doi.org/10.1016/j.virol.2023.04.014. Epub 20230605PubMed PMID: 37321144; PubMed Central PMCID: PMCPMC10240909.
Simon-Loriere, E., Schwartz, O., 2022. Towards SARS-CoV-2 serotypes? Nat. Rev. Microbiol. 20 (4), 187–188. https://doi.org/10.1038/s41579-022-00708-x. PubMed PMID: 35181769; PubMed Central PMCID: PMCPMC8855751.
Starr, T.N., Greaney, A.J., Addetia, A., Hannon, W.W., Choudhary, M.C., Dingens, A.S., et al., 2021. Prospective mapping of viral mutations that escape antibodies used to treat COVID-19. Science 371 (6531), 850–854. https://doi.org/10.1126/science.abf9302. Epub 20210125PubMed PMID: 33495308; PubMed Central PMCID: PMCPMC7963219.
Tamura, T., Ito, J., Uriu, K., Zahradnik, J., Kida, I., Anraku, Y., et al., 2023. Virological characteristics of the SARS-CoV-2 XBB variant derived from recombination of two Omicron subvariants. Nat. Commun. 14 (1), 2800. https://doi.org/10.1038/s41467-023-38435-3. Epub 20230516PubMed PMID: 37193706; PubMed Central PMCID: PMCPMC10187524.
Tao, K., Tzou, P.L., Nouhin, J., Gupta, R.K., de Oliveira, T., Kosakovsky Pond, S.L., et al., 2021. The biological and clinical significance of emerging SARS-CoV-2 variants. Nat. Rev. Gen. 22 (12), 757–773. https://doi.org/10.1038/s41576-021-00408-x. Epub 20210917PubMed PMID: 34535792; PubMed Central PMCID: PMCPMC8447121.
Tsai, K.C., Lee, Y.C., Tseng, T.S., 2021. Comprehensive deep mutational scanning reveals the immune-escaping hotspots of SARS-CoV-2 receptor-binding domain targeting neutralizing antibodies. Front. Microbiol. 12, 698365 https://doi.org/10.3389/fmicb.2021.698365. Epub 20210715PubMed PMID: 34335530; PubMed Central PMCID: PMCPMC8319916.
Uriu, K., Ito, J., Zahradnik, J., Fujita, S., Kosugi, Y., Schreiber, G., et al., 2023. Enhanced transmissibility, infectivity, and immune resistance of the SARS-CoV-2 Omicron XBB.1.5 variant. Lancet Infect. Dis. 23 (3), 280–281. https://doi.org/10.1016/S1473-3099(23)00051-8. Epub 20230131PubMed PMID: 36736338; PubMed Central PMCID: PMCPMC9889095.
van der Straten, K., Guerra, D., van Gils, M.J., Bontjer, I., Caniels, T.G., van Willigen, H.D.G., et al., 2022. Antigenic cartography using sera from sequence-confirmed SARS-CoV-2 variants of concern infections reveals antigenic divergence of Omicron. Immunity 55 (9), 1725–1731. https://doi.org/10.1016/j.immuni.2022.07.018 e4. Epub 20220805PubMed PMID: 35973428; PubMed Central PMCID: PMCPMC9353602.
Wan, Y., Shang, J., Graham, R., Baric, R.S., Li, F., 2020. Receptor recognition by the novel coronavirus from wuhan: an analysis based on decade-long structural studies of SARS coronavirus. J. Virol. 94 (7) https://doi.org/10.1128/JVI.00127-20. Epub 20200317PubMed PMID: 31996437; PubMed Central PMCID: PMCPMC7081895.
Wang, Q., Ye, S.B., Zhou, Z.J., Li, J.Y., Lv, J.Z., Hu, B., et al., 2023. Key mutations on spike protein altering ACE2 receptor utilization and potentially expanding host range of emerging SARS-CoV-2 variants. J. Med. Virol. 95 (1), e28116. https://doi.org/10.1002/jmv.28116. Epub 20220913PubMed PMID: 36056469; PubMed Central PMCID: PMCPMC9538830.
Winkler, E.S., Bailey, A.L., Kafai, N.M., Nair, S., McCune, B.T., Yu, J., et al., 2020. SARS-CoV-2 infection of human ACE2-transgenic mice causes severe lung inflammation and impaired function. Nat. Immunol. 21 (11), 1327–1335. https://doi.org/10.1038/s41590-020-0778-2. Epub 20200824PubMed PMID: 32839612; PubMed Central PMCID: PMCPMC7578095.
Yue, C., Song, W., Wang, L., Jian, F., Chen, X., Gao, F., et al., 2023. ACE2 binding and antibody evasion in enhanced transmissibility of XBB.1.5. Lancet Infect. Dis. 23 (3), 278–280. https://doi.org/10.1016/S1473-3099(23)00010-5. Epub 20230203PubMed PMID: 36746173; PubMed Central PMCID: PMCPMC9897732.
Zabidi, N.Z., Liew, H.L., Farouk, I.A., Puniyamurti, A., Yip, A.J.W., Wijesinghe, V.N., et al., 2023. Evolution of SARS-CoV-2 variants: implications on immune escape, vaccination, therapeutic and diagnostic strategies. Viruses 15 (4). https://doi.org/10.3390/v15040944. Epub 20230410PubMed PMID: 37112923; PubMed Central PMCID: PMCPMC10145020.

Zahradnik, J., Marciano, S., Shemesh, M., Zoler, E., Harari, D., Chiaravalli, J., et al., 2021. SARS-CoV-2 variant prediction and antiviral drug design are enabled by RBD *in vitro* evolution. Nat. Microbiol. 6 (9), 1188–1198. https://doi.org/10.1038/s41564-021-00954-4. Epub 20210816PubMed PMID: 34400835.

Zamorano Cuervo, N., Grandvaux, N, 2020. ACE2: evidence of role as entry receptor for SARS-CoV-2 and implications in comorbidities. eLife 9. https://doi.org/10.7554/eLife.61390. Epub 20201109PubMed PMID: 33164751; PubMed Central PMCID: PMCPMC7652413.

Zhang, W., Shi, K., Geng, Q., Herbst, M., Wang, M., Huang, L., et al., 2023. Structural evolution of SARS-CoV-2 omicron in human receptor recognition. J. Virol. 97 (8), e0082223 https://doi.org/10.1128/jvi.00822-23. Epub 20230814PubMed PMID: 37578233; PubMed Central PMCID: PMCPMC10506476.

Zheng, J., Wong, L.R., Li, K., Verma, A.K., Ortiz, M.E., Wohlford-Lenane, C., et al., 2021. COVID-19 treatments and pathogenesis including anosmia in K18-hACE2 mice. Nature 589 (7843), 603–607. https://doi.org/10.1038/s41586-020-2943-z. Epub 20201109PubMed PMID: 33166988; PubMed Central PMCID: PMCPMC7855185.

Zhou, P., Yang, X.L., Wang, X.G., Hu, B., Zhang, L., Zhang, W., et al., 2020. A pneumonia outbreak associated with a new coronavirus of probable bat origin. Nature 579 (7798), 270–273. https://doi.org/10.1038/s41586-020-2012-7. Epub 20200203PubMed PMID: 32015507; PubMed Central PMCID: PMCPMC7095418.